

Published in final edited form as:

J Magn Reson. 2014 July ; 244: 53–63. doi:10.1016/j.jmr.2014.04.016.

A framework for accurate determination of the T_2 distribution from multiple echo magnitude MRI images

Ruiliang Bai^{1,2}, Cheng Guan Koay³, Elizabeth Hutchinson¹, and Peter J. Basser¹

¹Section on Tissue Biophysics and Biomimetics, PPITS, NICHD, National Institutes of Health, Bethesda, MD 20892, USA

²Biophysics Program, Institute for Physical Science and Technology, University of Maryland, College Park, MD 20740 USA

³Department of Medical Physics, University of Wisconsin School of Medicine and Public Health, Madison, WI 53705 USA

Abstract

Measurement of the T_2 distribution in tissues provides biologically relevant information about normal and abnormal microstructure and organization. Typically, the T_2 distribution is obtained by fitting the magnitude MR images acquired by a multi-echo MRI pulse sequence using an inverse Laplace transform (ILT) algorithm. It is well known that the ideal magnitude MR signal follows a Rician distribution. Unfortunately, studies attempting to establish the validity and efficacy of the ILT algorithm assume that these input signals are Gaussian distributed. Violation of the normality (or Gaussian) assumption introduces unexpected artifacts, including spurious cerebrospinal fluid (CSF)-like long T_2 components; bias of the true geometric mean T_2 values and in the relative fractions of various components; and blurring of nearby T_2 peaks in the T_2 distribution. Here we apply and extend our previously proposed magnitude signal transformation framework to map noisy Rician-distributed magnitude multi-echo MRI signals into Gaussian-distributed signals with high accuracy and precision. We then perform an ILT on the transformed data to obtain an accurate T_2 distribution. Additionally, we demonstrate, by simulations and experiments, that this approach corrects the aforementioned artifacts in magnitude multi-echo MR images over a large range of signal-to-noise ratios.

Keywords

T_2 distribution; MRI; multi-echo; magnitude; Rician; Gaussian; signal; probability integral transform

Corresponding author: Ruiliang Bai, ruiliang.bai@nih.gov.

Publisher's Disclaimer: This is a PDF file of an unedited manuscript that has been accepted for publication. As a service to our customers we are providing this early version of the manuscript. The manuscript will undergo copyediting, typesetting, and review of the resulting proof before it is published in its final citable form. Please note that during the production process errors may be discovered which could affect the content, and all legal disclaimers that apply to the journal pertain.

1. Introduction

NMR relaxation measurements have been widely applied to study molecular dynamics in porous media [1,2], polymers and gels [3–5], food sciences [6], material sciences [7], plant tissue [8], and animal and human tissue studies [9,10]. NMR relaxometry, combined with MR imaging, is a powerful tool for characterizing the detailed microstructure of animal and human tissue *ex vivo* and *in vivo*, revealing complex microstructure in the brain [11–13], a layered structure in the cartilage [14], distinct domains in bone [15], etc.

Magnitude, rather than complex MRI signals, is widely used in quantitative MRI studies. This choice is primarily due to the fact that the phase of MRI signals is sensitive to many experimental factors, such as scanner type, field inhomogeneity, temperature, coil type, pulse sequence design, motion, etc. [16–19]. While magnitude MRI is preferred in relaxation experiments, the signal-to noise ratio (SNR) in MRI is usually much lower than in its NMR counterpart. Ideally, the distribution of the NMR and MRI signal is Rician rather than Gaussian [16,20,21]; this distribution can cause problems in estimating relaxation parameters accurately, such as the T_1 and T_2 in MRI [22,23], particularly as the MRI signal approaches the background noise levels.

Quantitative T_2 (qT_2) MRI spectroscopy has attracted more attention in recent years due to its ability to identify microstructure-dependent T_2 components empirically without invoking prior modeling assumptions [10,12,24–26]. Specifically, the T_2 distribution—a plot of component weightings as a function of T_2 —can provide information about the relative fraction of different distinct components in a material, such as the myelin water fraction within nerve samples. Calculated maps can yield potentially important biomarkers of pathology in demyelination diseases such as multiple sclerosis [13,24,27,28].

Typically, to obtain the T_2 distribution, a multi-echo MRI acquisition is performed on a single slice or multiple slices, and then the magnitude MRI data is directly fitted to an inverse Laplace transform (ILT) algorithm. This transformation is achieved by decomposing the signal into a sum of discrete exponential components, each with a unique relaxation time and amplitude. Estimates derived through ILT are generally sensitive to the presence of noise [23,29–31]. Furthermore, conventional ILT algorithms are based on least-squares methods that assume the signals are Gaussian distributed with a constant variance. Since the ideal magnitude MR signal is Rician distributed it is biased more toward a higher value than the noise-free signal intensity, while the signal variance is artificially decreased as the SNR approaches zero [20,21,23,32,33].

Specifically, noise in qT_2 MRI acquisitions can produce spurious cerebrospinal fluid (CSF)-like long T_2 components, bias of the true geometric mean T_2 (gmT_2) values and relative fractions of various components, and blurring of nearby T_2 peaks [33], all of which limit the accuracy of qT_2 MRI. Recently, a temporal phase correction algorithm was developed to separate the relevant decay information from the noisy complex signal into the real channel, leaving only noise in the imaginary channel [33]. Although this strategy may improve some aspects of qT_2 MRI, the phase of the complex MRI signal may differ on the basis of the equipment used (scanners, coils, etc. [16–19]). The magnitude of the complex MR signal

remains the most commonly used data in quantitative measures in MRI. Ideally, we would like to develop a scheme that maps the noisy magnitude MRI data to a Gaussian-distributed signal.

In our previous work, a signal transformation framework was proposed to map noisy Rician-distributed magnitude diffusion weighted MRI (DWI) signals into Gaussian-distributed DWI signals without using the phase information [32]. This framework has been applied successfully in quantitative diffusion MRI studies [32,34]. Generally, the first step includes estimation of noise variance and underlying signal, followed by transformation of the signal distribution to a Gaussian.

Here we adapt and extend this framework from DWI applications, most of which are model-based, to multi-echo qT_2 MRI spectral data that invokes no prior modeling assumptions. The artifacts in the T_2 distribution caused by the Rician MRI signals were systematically studied in simulations and real multi-echo MRI experiments within different SNR. The effectiveness of the modified signal transformational framework was investigated in this new application and our proposed framework was found to yield more accurate estimates of the T_2 distribution over a large range of SNR than direct use of magnitude MRI.

2. Methods

2.1. Distribution of the magnitude MR signals

It is well known that that using the magnitude of the Gaussian-distributed complex MRI data follows a Rician distribution, which is characterized by the following probability density function (PDF)[16,35]:

$$p(m|\eta, \sigma_g)dm = \frac{m}{\sigma_g^2} \exp\left(-\frac{\eta^2 + m^2}{\sigma_g^2}\right) I_0\left(\frac{m\eta}{\sigma_g^2}\right) dm, \quad (1)$$

where m is the noisy magnitude data, η is the underlying signal intensity, σ_g is the Gaussian noise standard deviation, and I_0 is the 0^{th} -order modified Bessel function of the first kind. The corresponding cumulative distribution function (CDF) can be expressed as [32]:

$$p_r(\alpha|\eta, \sigma_g) = \int_0^\alpha p(m|\eta, \sigma_g)dm = 1 - \int_\alpha^\infty p(m|\eta, \sigma_g)dm = 1 - Q(\eta/\sigma_g, \alpha/\sigma_g) \quad (2)$$

where Q is the generalized Marcum- Q function.

An important special limiting case of the Rician distribution is when the SNR ($\text{SNR} = \eta/\sigma_g$) is high enough that the PDF of Eq. (1) approaches the Gaussian distribution with a sample mean η and standard deviation σ_g [21]. Another important special case is when the underlying signal is zero, so that the Rician distribution in Eq. (1) reduces to a Rayleigh distribution [21]:

$$p_r(m|0, \sigma_g)dm = \frac{m}{\sigma_g^2} \exp\left(-\frac{m^2}{2\sigma_g^2}\right) dm. \quad (3)$$

2.2 The framework for accurate determination of the T_2 distribution from multi-echo magnitude MRI images

The framework we proposed to accurately estimate T_2 distribution from multi-echo magnitude MRI images is described in Fig. 1. There are four essential steps: 1) the variance of the noise is estimated taking advantage of the multidimensional data structure (2.2.1), 2) the underlying signal intensity is estimated using an adapted fixed point formula (2.2.2), 3) the estimated variance and underlying signal intensity are then used to transform the noisy magnitude signal to a noisy Gaussian-form signal by using the probability integral transform to match the cumulative distribution functions (2.2.3), and 4) an ILT algorithm is then performed on the transformed data to estimate the T_2 distribution for each voxel (2.2.4).

2.2.1 Estimation of the noise standard deviation (SD)—The accuracy of the noise variance estimation affects the accuracy of the estimate of the underlying signal intensity and of the transformed signal. Most current methods to estimate noise variance are based on applying the Rayleigh distribution [Eq. (3)] to fit the noise within a selected region of interest (ROI) on the magnitude MR image [16,35–38]. However, the additional information contained in the multi-dimensional data structures, such as the additional T_2 dimension in multi-echo MRI, provides an opportunity to use more advanced noise estimation approaches. Recently, we proposed a coherent framework for the probabilistic identification and estimation of noise (also known as PIESNO [39]). This approach was developed for the simultaneous identification of the noise-only pixels and estimation of the noise variance by taking advantage of the special data structure similar to multi-echo MRI for qT_2 . The method can be briefly described as follows.

For a measurement $m_{i,j,k}$, where i,j are the x - y spatial coordinates and k is the added experimental dimension, for example, different echo times with K measurements. Assuming that the Gaussian noise SD, σ_g , across the added dimension is uniform, we may write the sample mean $s_{i,j}$ as:

$$s_{i,j} = \frac{1}{K} \sum_{k=1}^K t_{i,j,k} = \frac{1}{2\sigma_g^2 K} \sum_{k=1}^K m_{i,j,k}^2. \quad (4)$$

If $s_{i,j}$ is in the acceptable range of the corresponding CDF of Eq. (3), the corresponding pixels along k will be designated noise only. This is a self-consistent method, where the collection of identified noise-only pixels will be used to determine the underlying Gaussian SD; then a new iteration begins in which the new estimate of the Gaussian SD is used in Eq. (4). The iteration continues until the Gaussian SD converges or the iteration reaches the maximum threshold.

2.2.2. A fixed point formula for the estimation of the underlying signal intensity—The estimation of the underlying signal intensity η follows the fixed point formula developed in our previous work [20,32] by finding the solution of the following equation:

$$\eta = g(\eta | \langle m \rangle, \sigma_g) = \sqrt{\langle m \rangle^2 + [\zeta(\eta | \sigma_g) - 2] \sigma_g^2} \quad (5)$$

where $\langle m \rangle$ is the first moment of m , which is estimated by smoothing the decay curve, and ζ is an analytical function of signal intensity η and noise SD σ_g . More details about Eq. (5) are summarized in Appendix A. This formula has been modified for qT₂ MRI application by assigning the underlying signal intensity η to be 0 rather than a negative value as in our previous framework when the estimated $\langle m \rangle$ is occasionally below the noise floor $\sqrt{\pi/2} \sigma_g$ when the SNR is close to 0 (see Appendix A).

2.2.3 Mapping the noisy magnitude signal to Gaussian distribution—Using the Gaussian SD σ_g and the underlying signal η estimated in Section 2.2.1 and 2.2.2, respectively, the corresponding CDF for measurement m can be calculated from Eq. (2). The inverse cumulative probability function of a Gaussian random variable and the cumulative probability function of noisy Rician magnitude signals using the probability integral transform [40,41] are then used to map from the noisy magnitude signal to a Gaussian form. The final transformed noisy Gaussian signal χ would be:

$$\chi = P_G^{-1}(P_r(m | \eta, \sigma_g) | \eta, \sigma_g) \quad (6)$$

where P_G^{-1} is the inverse cumulative distribution function of a Gaussian distribution. More details can be found in [32].

2.2.4. ILT algorithm—A non-negative least squares (NNLS) algorithm with Tikhonov regularization was then applied on the transformed relaxation decay signals [42,43]. In the absence of noise, the ideal T₂ relaxation decay curve can be described as a multi-exponential function:

$$\eta(t_k) = \eta_0 \sum_{n=1}^N F(T_{2,n}) \exp(-t_k/T_{2,n}), k=1, 2, \dots, K \quad (7)$$

where η_0 is the proton density, F is the probability function at each T₂ value and is assumed to be non-negative, t_k are the K echo times, and $T_{2,n}$ are the N logarithmically spaced T₂ time spacing. A robust and relatively stable solution of $F(T_{2,n})$ in the presence of noise can be obtained by minimizing Ξ

$$\Xi = \sum_{k=1}^K (\eta(t_k) - \chi_k)^2 + \mu \sum_{n=1}^N F(T_{2,n})^2 \quad (8)$$

where χ_k is the transformed signal χ at echo time t_k , and μ is the parameter controlling the Tikhonov regularization. A Butler-Reeds-Dawson (BRD) method [44] based on the Morozov discrepancy principle [45], which compares $d(\log_{10} \Xi)/d(\log_{10} \mu)$ against a user-defined tolerance, TOL [46], was used to robustly determine the value of μ .

2.3. Simulations of multi-echo MRI magnitude data

The decay curves of the multi-echo MRI magnitude data at different SNRs were simulated by Monte Carlo methods to explore their artifacts on qT_2 MR and the efficacy of our proposed framework in correcting them. The noisy multi-echo MRI magnitude signal m at echo time t_k was generated by the following function:

$$m_k = \sqrt{(\eta(t_k) + \varepsilon_1)^2 + \varepsilon_2^2} \quad (9)$$

where $\eta(t_k)$ is the ground truth calculated by Eq. (7) with targeted T_2 distribution and ε_1 and ε_2 are the Gaussian random variables with mean zero and targeted standard deviation. Two different T_2 distributions were explored to simulate different tissue properties: one contains only a single component with gmT_2 equal to 51.6ms; the other contains two components whose gmT_2 and weightings are (15.7ms, 50%) and (51.6ms, 50%). In both cases, the underlying T_2 distributions have a narrow Gaussian shape in the logarithmic T_2 space. The initial SNR ($iSNR \equiv \eta_0/\sigma_g$) ranges from 10 to 400 for single-component cases and from 30 to 410 for the double-component simulations.

In each simulation, 50 echo times TE were uniformly sampled from 5ms to 250ms with a gap of 5ms. The noisy magnitude data and their transformed signals were then analyzed to get the T_2 distributions using the ILT algorithm in Section 2.2.4. The T_2 distribution consisted of 50 T_2 bins logarithmically spaced between half of the shortest TE (2.5ms) and two times the longest TE (500ms). TOL in the BRD method was set to 0.003. To achieve stability in statistics, 1000 realizations were performed at each SNR level and each targeted T_2 distribution.

2.4 Multi-echo MRI experiments of a gel phantom and fixed spinal cord tissue

Two samples were prepared for MRI experiments: a composite agarose and $CuSO_4$ phantom and an excised porcine spinal cord. The phantom was made using a filled spherical insert in a 10mm NMR tube. Each sample was filled with a different $CuSO_4$ doped agar gel. The spherical insert was filled with 1% agar gel doped with 100mM $CuSO_4$ and the NMR tube was filled with 0.5% agar gel doped with 50mM $CuSO_4$. The porcine spinal cord was excised and immediately immersion fixed in a 4% formalin solution. The spinal cord was fully rehydrated with phosphate buffered saline (PBS) prior to the MRI experiments and then contained within a 10mm susceptibility-matching Shigemi tube (Shigemi Inc., Japan) with Fluorinert (3M, St. Paul, MN) filling the unoccupied space during the MRI experiments.

Multi-echo acquisitions were performed on a 7T Bruker Avance III vertical bore MRI scanner equipped with a micro2.5 gradient system (Bruker BioSpin, Billerica, MA). For both the gel phantom and the porcine spinal cord, a single slice was selected with 50 echoes starting at 7ms and continuing to 350ms in 7ms increments. The other acquisition parameters for the gel phantom were: TR = 2000ms, matrix size = 128×128, slice thickness = 0.2mm, FOV = 12mm×12mm, and repetitions = 50, and for the spinal cord were: TR = 3000ms, matrix size = 128×128, slice thickness = 1.00mm, FOV = 12mm×12mm, and

repetitions = 64. In both experiments, hermite pulse shapes were applied for both excitation and refocusing pulses with bandwidth (5400Hz) matching.

To achieve different SNR levels, the complex data were averaged using different numbers of repetitions from the whole set initially. The magnitude images were then processed according to the framework detailed in Section 2.2. The T_2 distribution also consisted of 50 T_2 bins logarithmically spaced between half of the shortest TE (3.5ms) and twice of the longest TE (700ms) with $TOL = 0.003$.

2.5 Analysis of the T_2 distributions

In the simulations, the T_2 distribution at each SNR level was determined by averaging the T_2 distributions of 1000 identical simulations with random noise. In the MRI experiments, ROIs were selected at first; then a T_2 distribution was calculated for each ROI by averaging the T_2 distributions for all of the voxels inside each ROI. In the phantom experiments, two ROIs were selected: one containing all of the shorter- T_2 gel and the second containing all of the longer- T_2 gel. In the spinal cord experiments, three ROIs (dorsal, lateral and ventral) in white matter (WM) and one ROI in gray matter (GM) with relative homogenous gmT_2 were selected for further analysis.

In both simulations and experiments, the T_2 distributions with a single component were divided into two regimes: 1) tissue-associated water, from the shortest T_2 bin to 200ms and 2) CSF-like water, from 200ms to the longest T_2 bin. As for the T_2 distributions with multiple components, the tissue-associated water was further divided into myelin water (MW, from the shortest T_2 bin to 27ms) and intracellular/extracellular water (IEW, from 27ms to 200ms).

3. Results

3.1. Validation of the framework

3.1.1 Estimation of the underlying Gaussian noise SD—To determine the accuracy of PIESNO in estimating the Gaussian noise SD from the multi-echo MRI data, both synthetic signals and the data from the experiments with porcine spinal cord were investigated. The synthetic signals contained the same data structure ($128 \times 128 \times 50$) as the signals in the single-slice multi-echo experiment on the spinal cord. The T_2 relaxation decay curve in each voxel was generated following Eq. (9) with the single-component T_2 distribution with gmT_2 equal to 51.6ms. The proton density η_0 was set to be 1 for the centered 64×64 square matrix and 0 for the other regions.

The values of estimated Gaussian noise SD were plotted against the known SD σ_g from 0.01 to 0.2 (arbitrary units) in Fig. 2A, and it was found that the estimated values deviated less than 0.3% from the known values. In the spinal cord experiments, the underlying Gaussian noise SD in different SNRs was also estimated via PIESNO. The different SNRs were achieved by averaging the complex data with a step of two. The estimated Gaussian SD (Fig. 2B) was well fitted with the expected function:

$$\sigma_g(N) = \sigma_{g,0} / \sqrt{N} \quad (10)$$

via the non-linear least squares method with $R^2 = 0.9999$.

3.1.2 Signal transformation from Rician distribution to Gaussian distribution—

The efficacy of the proposed framework in correcting the multi-echo MRI magnitude data was validated by performing Monte Carlo simulations similar to those in Section 3.2 of [32]. 50,000 sets of the simulations described in Section 2.3 with a single T_2 ($gmT_2 = 51.6\text{ms}$) were performed with the following parameters: proton density $\eta_0 = 1000$, TE ranges from 5ms to 250ms with a gap of 5ms, and Gaussian noises with mean zero and SD = 100 in real and imaginary channels.

In Fig. 3A, the sample mean and sample SD of the 50,000 measurements at each TE are shown, where the maximum offset caused by the nature of the Rician distribution can be 117 from the ground truth as the SNR approaches 0. The underestimation problem of our original framework becomes apparent when the TE s are longer than 100ms, with a corresponding SNR of 1.5 (Fig. 3B). In our current framework (Fig. 3C), the maximum distance and the mean distance between the sample mean of the transformed signals and the ground truth of all the TE s were reduced from 30 to 19 and from 14 to 5 (arbitrary units) compared with our previous framework. The SD of the Rician signals is far from the ground truth (100); it can be up to 35% lower than the ground truth as SNR approaches 0 (Fig. 3D). As for the transformed signals, the maximum and mean biasing of the variances' SD from the ground truth were 56% and 14% higher in our previous framework and only 16% and 5% higher in our current framework.

The histograms of the noisy magnitude signals and their transformed values via the scheme proposed here at $TE = 200\text{ms}$ are shown in Fig. 4A and Fig. 4B. The noisy magnitude data have a sample mean of 126 and a sample SD of 66, while the transformed signal was successfully corrected back to a Gaussian distribution ($p > 0.1$ for any random 2000 samples) with a sample mean of 15 and a sample SD of 108, where the ground truth is 22 and the SD 100. Similar histograms of the shorter T_2 gel at $TE = 140\text{ms}$ are also shown in Fig. 4C and Fig. 4D. The noisy magnitude intensity was well fit with a Rician distribution (red curve) with sample mean and SD equal to 2.5×10^4 and 1.3×10^4 , while the transformed signal was successfully described by a Gaussian distribution ($p = 0.96$) with sample mean and SD equal to $(7.3 \times 10^3$ and $2.0 \times 10^4)$, where the ground truth is 5.8×10^3 with an SD of 1.9×10^4 (the results from the data with 50 averages).

3.2. Simulations of qT_2 MRI experiments

3.2.1 Simulations of the T_2 distribution with a single T_2 component—A

demonstration of the effects of signal transformation on the T_2 distribution with an initial SNR (iSNR) equal to 25 is shown in Fig. 5. There is a clear offset in the magnitude signal when the underlying signal is approaching zero, which is reflected in the T_2 distribution as a tail in the CSF-like regime (relative fraction 2.5%). This offset in the magnitude signal also causes the tissue-associated peak (51.6ms) to occur at a shorter relaxation time (46.6ms).

When the transformed signal is used in the NNLS algorithm, the spurious CSF-like tail disappears and the tissue-associated peak is corrected back to 50.9ms.

The statistical results of estimating T_2 distributions with various iSNR are shown in Fig. 6. Apparently, the bias of the tissue-associated water peak worsens as SNR goes down (Fig. 6A), while the proposed signal transformation makes the T_2 distributions more consistent over the entire range of SNR (Fig. 6C). Even at the lowest iSNR (iSNR=10), the gm T_2 and relative fraction of the tissue-associated water are successfully corrected from (32.8ms, 91.4%) to (40.3ms, 99.1%), where the ground truth is (51.6ms, 100%). To achieve the relative fraction of the spurious CSF-like water less than 1% of the total water, an iSNR higher than 50 is necessary using the Rician signal directly; however, iSNR \geq 10 is sufficient with our proposed framework.

3.2.2 Simulations of the T_2 distributions with two T_2 components—In Fig. 7A, the averaged T_2 distribution of each 1000 realizations with the original Rician signals (green) and transformed signals (blue) are shown against the ground truth with different iSNRs. Except for the generation of the spurious CSF-like water, the gm T_2 of both MW and IEW and the relative fraction of MW are underestimated, and the relative fraction of IEW is overestimated, especially when iSNR goes down (Fig. 7B and Fig. 7C). At iSNR=30, the estimated gm T_2 of the MW and IEW via directly fitting the Rician signals are 40.5% and 35.8% less than the ground truth, respectively, their relative fractions are 33.1% less and 38.5% higher than the ground truth. By implementing the proposed framework, the accuracy of both the gm T_2 and relative fraction estimations are improved. For example, to achieve 90% accuracy of the estimation of the MW fraction, iSNR \geq 110 is required when the Rician signals are used directly, while only iSNR \geq 50 is required when our proposed framework is implemented.

In Fig. 7A, at iSNR=30, the T_2 distribution calculated from the Rician signals only has one component in the tissue-associated water regime with gm T_2 =20.8ms and the relative fraction equal to 97.0%. In the T_2 distribution derived from the transformed signals, although the MW and IEW are still not clearly separable, the amplitude of $F(T_2)$ at the MW peak (T_2 =15.7ms) position is 96% higher than that derived from the Rician signals. At iSNR=50, the peaks of MW and IEW are still blurred in the T_2 distribution calculated from the Rician signals, but they become visible in the T_2 distribution derived from the transformed signals, where the minimum amplitude between the two peaks is already 43% less than the amplitude of the smaller peak. At higher iSNRs (>50), the MW and IEW are separable in both T_2 distributions. However, the position and the relative fraction of each component approach the ground truth faster via the transformed signals as the iSNR increases.

3.3. Experiment Results

3.3.1 Agar gel phantom—The images of the CSF-like water fraction from the data with 1, 4, 16 and 50 averages (corresponding iSNR=18,35,70,125) are shown in Fig. 8A. Our proposed framework decreases the spurious CSF-like water fraction from 3.5% to 0.6% for the shorter- T_2 gel and from 4.3% to 0.6% for the longer- T_2 gel when iSNR=18. Similar to the simulations with a single T_2 component, an iSNR of no less than 70 is required to

achieve 99% accuracy of the tissue-associated water fraction if the magnitude data are used with the NNLS algorithms directly, while the requirement of iSNR can be decreased to 18 by implementing our proposed framework.

The gmT_2 values of both gels were also corrected to more accurately reflect the ground truth: the gmT_2 of the shorter- T_2 gel was corrected from 24.8ms to 27.5ms at iSNR=18 where the ground truth is 28.7ms, and for the longer- T_2 gel from 57.5ms to 63.1ms where the ground truth is 63.9ms. More results with various iSNR are reported in Table 1.

3.3.2 Spinal cord—Maps of the gmT_2 of the entire T_2 distribution from 3.5ms to 700ms with the highest SNR are shown in Fig. 9A. Not surprisingly, the GM shows a longer gmT_2 than the WM. Anatomy-related inhomogeneity of the gmT_2 is shown in both GM and WM, which agrees with other studies on spinal cords [47,48]. In Fig. 9B, the WM ROIs show two clear relaxation components with the gmT_2 and relative fraction (20.1ms 62.3%, 59.1ms 37.6%) for ventral WM, (17.8ms 67.0%, 49.4ms 33.0%) for lateral WM, and (17.8ms 65.0%, 46.6ms 35.0%) for dorsal WM, while the GM ROI shows a single T_2 component with a broad shape, whose gmT_2 and relative fraction were (40.7ms 100.0%).

The development of the pattern of T_2 distributions under various SNR levels in each WM ROI matches the simulations of the two T_2 components in Section 3.2.2, where the blurring of the MW and IEW peaks worsens as the SNR diminishes. For example, at the lowest SNR (iSNR=30), the MW peak and IEW peak of the ventral WM merge into a single peak with the averaged gmT_2 values (28.1ms) of the two components, while the two components were clearly visible when the transformed signals were used (smallest amplitude between the two components is 64% of the smaller component's amplitude) with (17.4ms, 45.3%) for the MW and (46.5ms, 54.4%) for the IEW. More detailed SNR dependence for ventral WM are shown in Fig. 9C.

Consequently, the gmT_2 values and relative fractions of each regime are misestimated when the SNR is low; our framework makes these estimations more accurately. For example, our framework corrects the underestimation of the gmT_2 value and the overestimation of the relative fraction of the IEW in the ventral WM from 33.8% to 18.1% and from 63.8% to 44.7% at iSNR=30. To achieve 90% accuracy for the MW fraction estimation, our framework decreases the requirement of iSNR from 104 to 73.

Fig. 10 shows the relative fraction of the MW, IEW, and CSF in the spinal cord with 1, 4, 16, and 64 averages of the complex data. The overestimation of the IEW fraction and underestimation of the WM fraction are more serious in the ventral WM, which has a longer gmT_2 for the MW. Clearly the CSF fraction is overestimated and the contrast between GM and WM is not accurate. The latter is due both to the overestimation of the CSF, which is SNR dependent as illustrated in Fig. 6, Fig. 7, and Table 1, and to the fact that GM has a higher SNR than does WM. Our framework reduces not only the overestimation of the CSF fraction in both WM and GM but also the spurious contrast between the two.

4. Discussion

In this work, our main objective is to adapt and extend our original signal transformational framework for qT_2 MRI spectral data and to determine its efficacy in transforming the Rician magnitude signals from multi-echo MRI experiments to Gaussian-distributed signals with the hope of improving the accuracy of the estimation of the T_2 distribution.

The additional dimension (T_2 dimension) of the multi-echo MRI data provides a much larger sample to estimate the Gaussian standard deviation; this larger sample improves the precision of the Gaussian noise SD estimation within PIESNO. As a consequence, the precision of the underlying signal intensity estimate also improves.

Both the multi-echo MRI simulations and agar gel phantom experiments clearly illustrate the efficacy of our proposed framework in mapping the noisy Rician signals to noisy Gaussian signals, with nearly constant SDs. The underestimation of the signal intensity in the very low SNR regime in our original framework has been ameliorated by adding a non-negative boundary in the fixed-point formula to estimate the underlying signal intensity, where the variance of the transformed signals are more stable. However, we believe further studies are still needed to investigate the best scheme to address a sample mean of the magnitude signals that is below the noise floor.

Our results confirm that the artifacts in the T_2 distribution arise from the magnitude data mentioned in the literature [23,33] and illustrate their dependence on SNR. These artifacts include the generation of spurious CSF-like long T_2 tails, bias of the tissue-associated water peaks, blurring of nearby but distinct T_2 components, underestimation of the gmT_2 and relative fraction of myelin water, underestimation of the gmT_2 and overestimation of the relative fraction of intracellular/extracellular water. By implementing our proposed framework, the magnitude signals are transformed to meet the requirements of most ILT algorithms: that they be Gaussian distributed and have a constant standard deviation. As a consequence of this transformation, the associated artifacts of Rician signals are eliminated and the accuracy of the T_2 distribution is significantly improved.

It should be mentioned that the MW fraction of the porcine spinal cord used in this work (50%–70%) is higher than that found in other literature on rat spinal cord (10%–40%) [28,47,49]. To the best of our knowledge, no other quantitative study on the MW fraction of porcine spinal cord has been undertaken thus far. The larger MW fraction here may be the result of the differences between the two species or the different sample preparation procedures. As for GM, except for the correction of the biasing of the tissue-associated water and the generation of the spurious CSF components (see Fig. 9B), even the shape of T_2 distribution after implementation of our framework is more consistent over the entire range of SNR, though the underlying biophysical basis of this broad peak is still not clear.

Although SNR is still required to produce an accurate T_2 distribution, our framework decreases the SNR needed and improves the T_2 distribution over the entire range of SNR. Another advantage of our framework is its robustness; it does not require phase information and can be applied to the multi-echo MRI magnitude data from all preclinical and clinical

scanners (although other sources of noise, such as motion and physiological noise for *in vivo* applications, should be handled before using this framework).

The framework outlined in this work only illustrates the applications on multi-echo MRI data from a single transmit-receive RF coil. A similar framework can be adapted for a multi-receiver MRI system based on our original work on a multi-receiver MRI system with parallel imaging [32,39].

5. Conclusions

A modified signal transformational framework has been successfully applied to multi-echo MRI magnitude data without the need for any information on the phase. After transformation, the noisy magnitude signal was mapped back to a noisy Gaussian-distributed signal with a consistent and constant standard deviation. Our simulations and experimental results demonstrated that our proposed framework could significantly correct artifacts in the T_2 distribution caused by noisy Rician magnitude signals, including spurious CSF-like long T_2 components, biasing of the T_2 components and overestimation/underestimation of their relative fractions, and the blurring of two nearby distinct T_2 components. More importantly, this general framework should work robustly for all multi-echo MRI magnitude data through the entire range of SNR; this range makes the method practical for preclinical and clinical applications.

Acknowledgments

This work was supported by the Intramural Research Program of the Eunice Kennedy Shriver National Institute of Child Health and Human Development, NIH. Thanks to Mr. R. R. Clevenger, Mr. T. J. Hunt, Mrs. Joni Taylor from LAMS, NHLBI for obtaining the spinal cord specimens and Ms. L. Salak for editing the manuscript. We are also grateful to our colleagues Dr. M. E. Komlosch for assistance with the experiments and preparing samples and Dr. A. Avram for useful discussions.

Appendix A: A fixed point formula for the estimation of the underlying signal intensity

The first step of the estimation is writing the first and the second moments of magnitude MRI signal m [20,22,50,51]:

$$\langle m \rangle = \frac{1}{2\sigma_g^2} \left(\exp\left(-\frac{\eta^2}{4\sigma_g^2}\right) \sqrt{\frac{\pi}{2}} \sigma_g \left[(\eta^2 + 2\sigma_g^2) I_0\left(\frac{\eta^2}{4\sigma_g^2}\right) + \eta^2 I_1\left(\frac{\eta^2}{4\sigma_g^2}\right) \right] \right) \quad (\text{A.1})$$

$$\langle m^2 \rangle = 2\sigma_g^2 + \eta^2 \quad (\text{A.2})$$

Then the variance of the noisy magnitude data is expressed as a product of a scaling factor and the squares of the Gaussian SD :

$$\sigma_r^2 = \langle m^2 \rangle - \langle m \rangle^2 = \zeta(\eta|\sigma_g) \sigma_g^2 \quad (\text{A.3})$$

where the scaling factor ζ is an analytical function of SNR, i.e., $\theta \equiv \eta/\sigma_g$ [20]:

$$\zeta(\theta)=2+\theta^2-\frac{\pi}{8}\exp\left(-\frac{\theta^2}{2}\right)\left((2+\theta^2)I_0\left(\frac{\theta^2}{4}\right)+\theta^2I_1\left(\frac{\theta^2}{4}\right)\right)^2 \quad (\text{A.4})$$

By substituting Eq. (A.3) for Eq. (A.4), the underlying signal intensity can be estimated by finding the solution of this fixed-point equation:

$$\eta=g(\eta|\langle m \rangle, \sigma_g)=\sqrt{\langle m \rangle^2+[\zeta(\eta|\sigma_g)-2]\sigma_g^2} \quad (\text{A.5})$$

where the Gaussian SD, σ_g , is estimated by PIESNO, the method discussed in Section 2.2.1. Specifically, the underlying signal intensity η is estimated as follows:

First, the decay data are smoothed using a penalized spline model, whose degree of freedom was chosen based on the method of generalized cross-validation (GCV) (see Appendices A and C of [32]). Next, the smoothed estimate \hat{m} is substituted for $\langle m \rangle$ in Eq. (A.5), and the unique solution $\hat{\eta}$ is determined for $\hat{m} \geq \sqrt{\pi/2}\sigma_g$, where $\sqrt{\pi/2}\sigma_g$ is the level of the noise floor, for which the underlying signal intensity is 0 but the first moment of the Rician distribution, $\langle m \rangle$, is non-zero. When the estimated \hat{m} is below the noise floor, the underlying signal intensity is assigned to be 0.

In our original framework [32], the estimate $\hat{\eta}$ was made to be $-\hat{\eta}_g$ when the estimated \hat{m} is below the noise floor, where $\hat{\eta}_g$ is the signal intensity estimate obtained by solving a new equation, $\langle m \rangle = 2\sqrt{\pi/2}\sigma_g - \hat{m}$, to ensure the symmetry of the resultant distribution of $\hat{\eta}$ at zero SNR. However, the negative assignment of $\hat{\eta}$ biases the mean of the transformed noisy Gaussian signal by underestimating the ground truth signal when the SNR is close to 0 but not at 0 (around 0.15–2.0, see Section 3.2 in [32] and Fig. 3 in this paper). Unfortunately, the last several echoes of multi-echo MRI usually occur in this very low SNR regime rather than reaching zero. To improve the estimation of the underlying signal intensity in this very low SNR regime, rather than ensuring the symmetry at zero SNR, $\hat{\eta}$ was assigned to be 0 whenever $\hat{m} < \sqrt{\pi/2}\sigma_g$. We adopt this assignment of $\hat{\eta}$ based on the physical requirement that the variable η be non-negative for typical multi-echo MRI experiments. The effect of this modification is shown in Fig 3.

References

1. Song Y-Q. Focus on the physics of magnetic resonance on porous media. *New J. Phys.* 2012; 14:055017.
2. Britton MM, Graham RG, Packer KJ. Relationships between flow and NMR relaxation of fluids in porous solids. *Magn. Reson. Imaging.* 2001; 19:325–331. [PubMed: 11445307]
3. Colsonet R, Mariette F, Cambert M. NMR relaxation and water self-diffusion studies in whey protein solutions and gels. *J. Agric. Food Chem.* 2005; 53:6784–6790. [PubMed: 16104800]
4. Bai R, Bassar PJ, Briber RM, Horkay F. NMR water self-diffusion and relaxation studies on sodium polyacrylate solutions and gels in physiologic ionic solutions. *J. Appl. Polym. Sci.* 2014; 131:1–7.
5. Ghoshal S, Mattea C, Denner P, Stapf S. Heterogeneities in gelatin film formation using single-sided NMR. *J. Phys. Chem.B.* 2010; 114:16356–16363. [PubMed: 21086961]

6. Hills, B. Magnetic Resonance Imaging in Food Science. New York: Wiley; 1998.
7. Blumich, B. NMR Imaging of Materials. Oxford: Oxford University Press; 2000.
8. Snaar JEM, Van As H. Probing water compartments and membrane permeability in plant cells by ¹H NMR relaxation measurements. *Biophys. J.* 1992; 63:1654–1658. [PubMed: 19431868]
9. Harrison R, Bronskill MJ, Mark R, Henkelman M. Magnetization transfer and T2 relaxation components in tissue. *Magn. Reson. Med.* 1995; 33:490–496. [PubMed: 7776879]
10. Bakker CJG, Vriend J. Multi-exponential water proton spin-lattice relaxation in biological tissues and its implications for quantitative NMR imaging. *Phys. Med. Biol.* 1984; 29:509–518. [PubMed: 6330769]
11. Deoni SCL, Peters TM, Rutt BK. High-resolution T1 and T2 mapping of the brain in a clinically acceptable time with DESPOT1 and DESPOT2. *Magn. Reson. Med.* 2005; 53:237–241. [PubMed: 15690526]
12. MacKay A, Laule C, Vavasour I, Bjarnason T, Kolind S, Mädler B. Insights into brain microstructure from the T2 distribution. *Magn. Reson. Imaging.* 2006; 24:515–525. [PubMed: 16677958]
13. Laule C, Vavasour IM, Kolind SH, Li DKB, Traboulsee TL, Moore GRW, et al. Magnetic resonance imaging of myelin. *Neurotherapeutics.* 2007; 4:460–484. [PubMed: 17599712]
14. Xia Y. Relaxation anisotropy in cartilage by NMR microscopy (μ MRI) at 14- μ m resolution. *Magn. Reson. Med.* 1998; 39:941–949. [PubMed: 9621918]
15. Eckstein F, Burstein D, Link TM. Quantitative MRI of cartilage and bone: degenerative changes in osteoarthritis. *NMR Biomed.* 2006; 19:822–854. [PubMed: 17075958]
16. Henkelman RM. Measurement of signal intensities in the presence of noise in MR images. *Med. Phys.* 1985; 12:232. [PubMed: 4000083]
17. Ahn CB, Cho ZH. A new phase correction method in NMR imaging based on autocorrelation and histogram analysis. *IEEE Trans. Med. Imaging.* 1987; 6:32–36. [PubMed: 18230424]
18. Pipe JG. Motion correction with PROPELLER MRI: application to head motion and free-breathing cardiac imaging. *Magn. Reson. Med.* 1999; 42:963–969. [PubMed: 10542356]
19. Buonocore MH, Gao L. Ghost artifact reduction for echo planar imaging using image phase correction. *Magn. Reson. Med.* 1997; 38:89–100. [PubMed: 9211384]
20. Koay CG, Basser PJ. Analytically exact correction scheme for signal extraction from noisy magnitude MR signals. *J. Magn. Reson.* 2006; 179:317–322. [PubMed: 16488635]
21. Gudbjartsson H, Patz S. The Rician distribution of noisy MRI data. *Magn. Reson. Med.* 1995; 34:910–914. [PubMed: 8598820]
22. Karlsten OT, Verhagen R, Bovée WM. Parameter estimation from Rician-distributed data sets using a maximum likelihood estimator: application to T1 and perfusion measurements. *Magn. Reson. Med.* 1999; 41:614–623. [PubMed: 10204887]
23. Bjarnason TA, McCreary CR, Dunn JF, Mitchell JR. Quantitative T2 analysis: the effects of noise, regularization, and multivoxel approaches. *Magn. Reson. Med.* 2010; 63:212–217. [PubMed: 20027599]
24. Mackay A, Whittall K, Adler J, Li D, Paty D, Graeb D. In vivo visualization of myelin water in brain by magnetic resonance. *Magn. Reson. Med.* 1994; 31:673–677. [PubMed: 8057820]
25. Gersonde K, Felsberg L, Tolxdorff T, Ratzel D, Ströbel B. Analysis of multiple T2 proton relaxation processes in human head and imaging on the basis of selective and assigned T2 values. *Magn. Reson. Med.* 1984; 1:463–477. [PubMed: 6571570]
26. Peled S, Cory DG, Raymond SA, Kirschner DA, Jolesz A. Water diffusion, T2, and compartmentation in frog sciatic nerve. *Magn. Reson. Med.* 1999; 42:911–918. [PubMed: 10542350]
27. McCreary CR, Bjarnason TA, Skihar V, Mitchell JR, Yong VW, Dunn JF. Multiexponential T2 and magnetization transfer MRI of demyelination and remyelination in murine spinal cord. *Neuroimage.* 2009; 45:1173–1182. [PubMed: 19349232]
28. Minty EP, Bjarnason TA, Laule C, MacKay AL. Myelin water measurement in the spinal cord. *Magn. Reson. Med.* 2009; 61:883–892. [PubMed: 19191283]

29. Prange M, Song Y-Q. Understanding NMR T2 spectral uncertainty. *J. Magn. Reson.* 2010; 204:118–123. [PubMed: 20223689]
30. Callaghan PT, Arns CH, Galvosas P, Hunter MW, Qiao Y, Washburn KE. Recent Fourier and Laplace perspectives for multidimensional NMR in porous media. *Magn. Reson. Imaging.* 2007; 25:441–444. [PubMed: 17466759]
31. Fenrich FR, Beaulieu C, Allen PS. Relaxation times and microstructures. *NMR Biomed.* 2001; 14:133–139. [PubMed: 11320538]
32. Koay CG, Özarslan E, Basser PJ. A signal transformational framework for breaking the noise floor and its applications in MRI. *J. Magn. Reson.* 2009; 197:108–119. [PubMed: 19138540]
33. Bjarnason TA, Laule C, Bluman J, Kozlowski P. Temporal phase correction of multiple echo T2 magnetic resonance images. *J. Magn. Reson.* 2013; 231:22–31. [PubMed: 23563572]
34. Özarslan E, Shepherd TM, Koay CG, Blackband SJ, Basser PJ. Temporal scaling characteristics of diffusion as a new MRI contrast: Findings in rat hippocampus. *Neuroimage.* 2012; 60:1380–1393. [PubMed: 22306798]
35. Bernstein MA. Improved detectability in low signal-to-noise ratio magnetic resonance images by means of a phase-corrected real reconstruction. *Med. Phys.* 1989; 16:813. [PubMed: 2811764]
36. Edelstein WA. A signal-to-noise calibration procedure for NMR imaging systems. *Med. Phys.* 1984; 11:180. [PubMed: 6727793]
37. Chang, L-C.; Rohde, GK.; Pierpaoli, C. An automatic method for estimating noiseinduced signal variance in magnitude-reconstructed magnetic resonance images. In: Fitzpatrick, JM.; Reinhardt, JM., editors. *Med. Imaging, International Society for Optics and Photonics.* 2005. p. 1136-1142.
38. Sijbers J, Poot D, den Dekker AJ, Pintjens W. Automatic estimation of the noise variance from the histogram of a magnetic resonance image. *Phys. Med. Biol.* 2007; 52:1335–1348. [PubMed: 17301458]
39. Koay CG, Özarslan E, Pierpaoli C. Probabilistic Identification and Estimation of Noise (PIESNO): A self-consistent approach and its applications in MRI. *J. Magn. Reson.* 2009; 199:94–103. [PubMed: 19346143]
40. Liu P-L, Der Kiureghian A. Multivariate distribution models with prescribed marginals and covariances. *Probabilistic Eng. Mech.* 1986; 1:105–112.
41. van Albada SJ, Robinson PA. Transformation of arbitrary distributions to the normal distribution with application to EEG test-retest reliability. *J. Neurosci. Methods.* 2007; 161:205–211. [PubMed: 17204332]
42. Whittall KP, MacKay AL. Quantitative interpretation of NMR relaxation data. *J. Magn. Reson.* 1989; 84:134–152.
43. Lawson, CL.; Hanson, RJ. *Solving Least Squares Problems.* Englewood Cliffs, NJ: Prentice-Hall; 1974.
44. Butler JP, Reeds JA, Dawson SV. Estimating solutions of first kind integral equations with nonnegative constraints and optimal smoothing. *SIAM J. Numer. Anal.* 1981; 18:381–397.
45. Morozov, VA. *Methods for Solving Incorrectly Posed Problems.* New York, NY: Springer New York; 1984.
46. Fordham EJ, Sezginer A, Hall LD. Imaging multiexponential relaxation in the (y, LogeT1) plane, with application to clay filtration in rock cores. *J. Magn. Reson. Ser. A.* 1995; 113:139–150.
47. Dula AN, Gochberg DF, Valentine HL, Valentine WM, Does MD. Multiexponential T2, magnetization transfer, and quantitative histology in white matter tracts of rat spinal cord. *Magn. Reson. Med.* 2010; 63:902–909. [PubMed: 20373391]
48. Komlos ME, Özarslan E, Lizak MJ, Horkayne-Szakaly I, Freidlin RZ, Horkay F, et al. Mapping average axon diameters in porcine spinal cord white matter and rat corpus callosum using d-PFG MRI. *Neuroimage.* 2013; 78:210–216. [PubMed: 23583426]
49. Kozlowski P, Liu J, Yung AC, Tetzlaff W. High-resolution myelin water measurements in rat spinal cord. *Magn. Reson. Med.* 2008; 59:796–802. [PubMed: 18302247]
50. Rice SO. Mathematical analysis of random noise. *Bell Syst. Tech. J.* 1944; Vol. 23:282–332. P. 282-332.23.

51. Sijbers J, den Dekker AJ. Maximum likelihood estimation of signal amplitude and noise variance from MR data. *Magn. Reson. Med.* 2004; 51:586–594. [PubMed: 15004801]

Highlights

1. A framework transforms magnitude multi-echo MRI signals to Gaussian distributed.
2. Accurate T_2 distribution estimation is achieved using the transformed signals.
3. Spurious cerebrospinal fluid peak in the T_2 distribution is eliminated.
4. The blurring of two nearby distinct T_2 components is corrected.
5. The quantitative estimation of T_2 -related parameters is more precise.

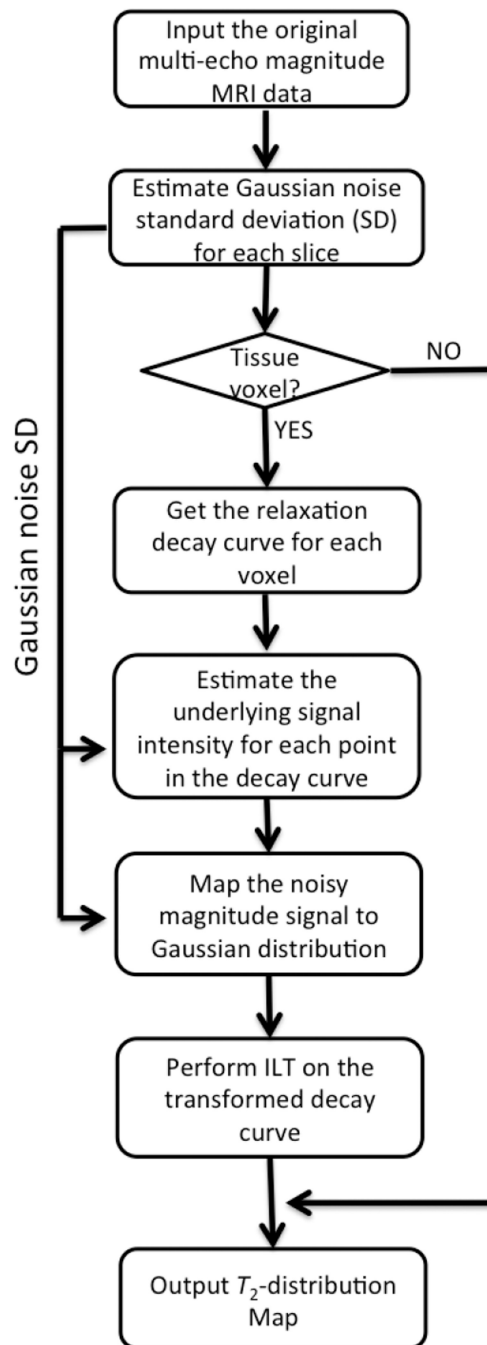


Fig. 1.
Framework to determine the T_2 distribution for each voxel.

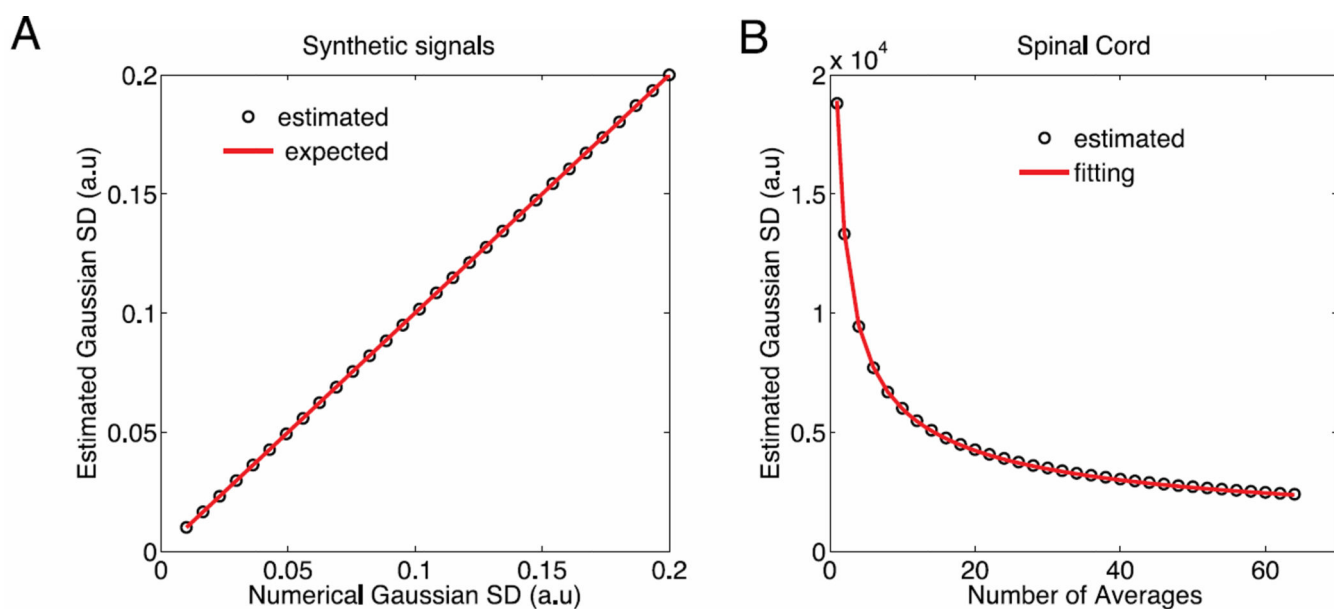
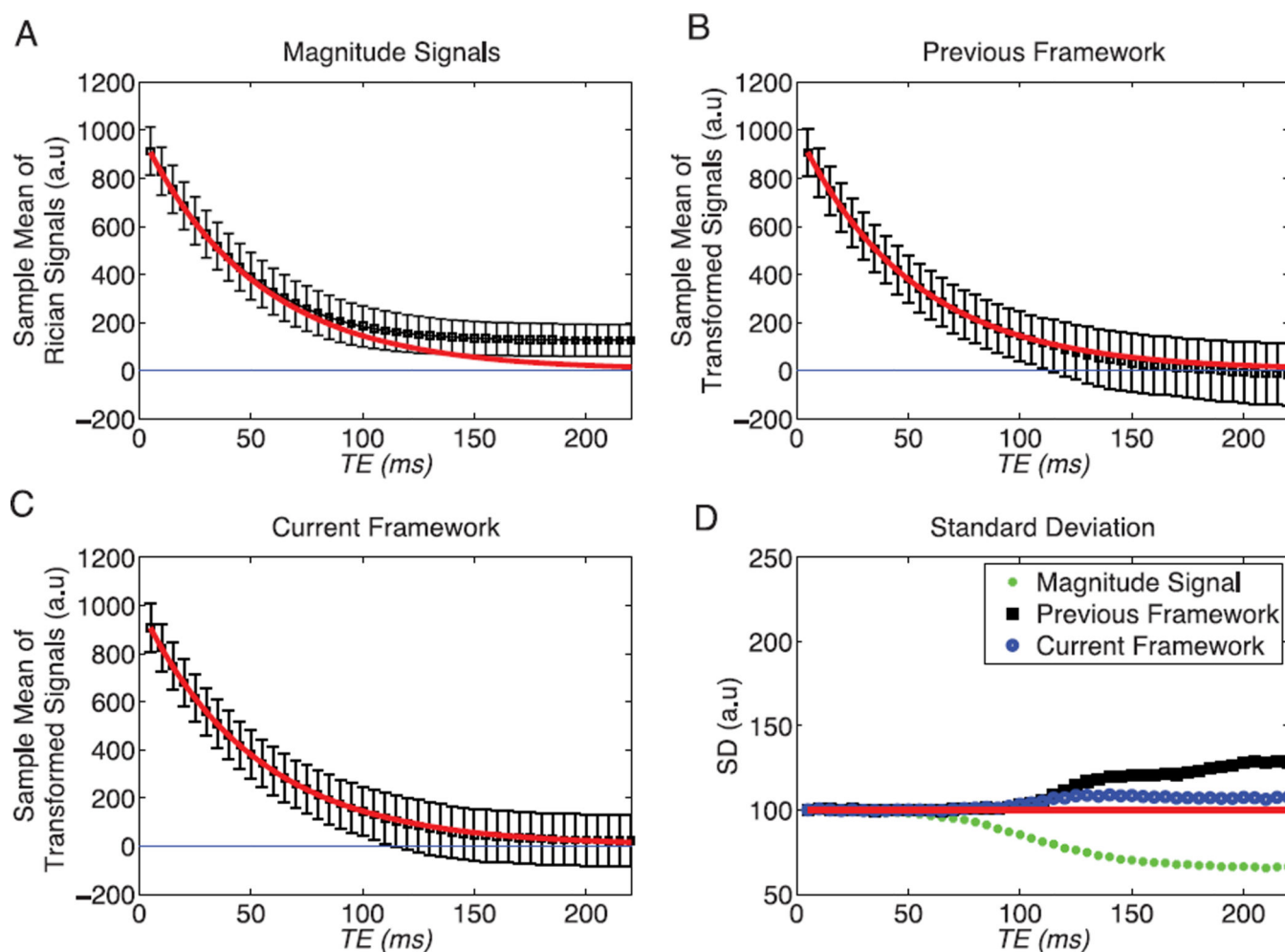


Fig. 2.

The estimated Gaussian SD via PIESNO from the synthetic signals with various noise levels (A) and from the spinal cord multi-echo MRI experiments with various averaging steps (B), where the red curve is the non-linear fit of the data via Eq. (10).

**Fig. 3.**

The black box and the error bar at each TE are the sample mean and the sample standard deviation of the noisy magnitude signals (A), the transformed signals via our previous framework (B), and the proposed modified framework here (C). The red continuous curves in (A–C) are the ground truth. The sample SD of the three sets of signals at each TE (D).

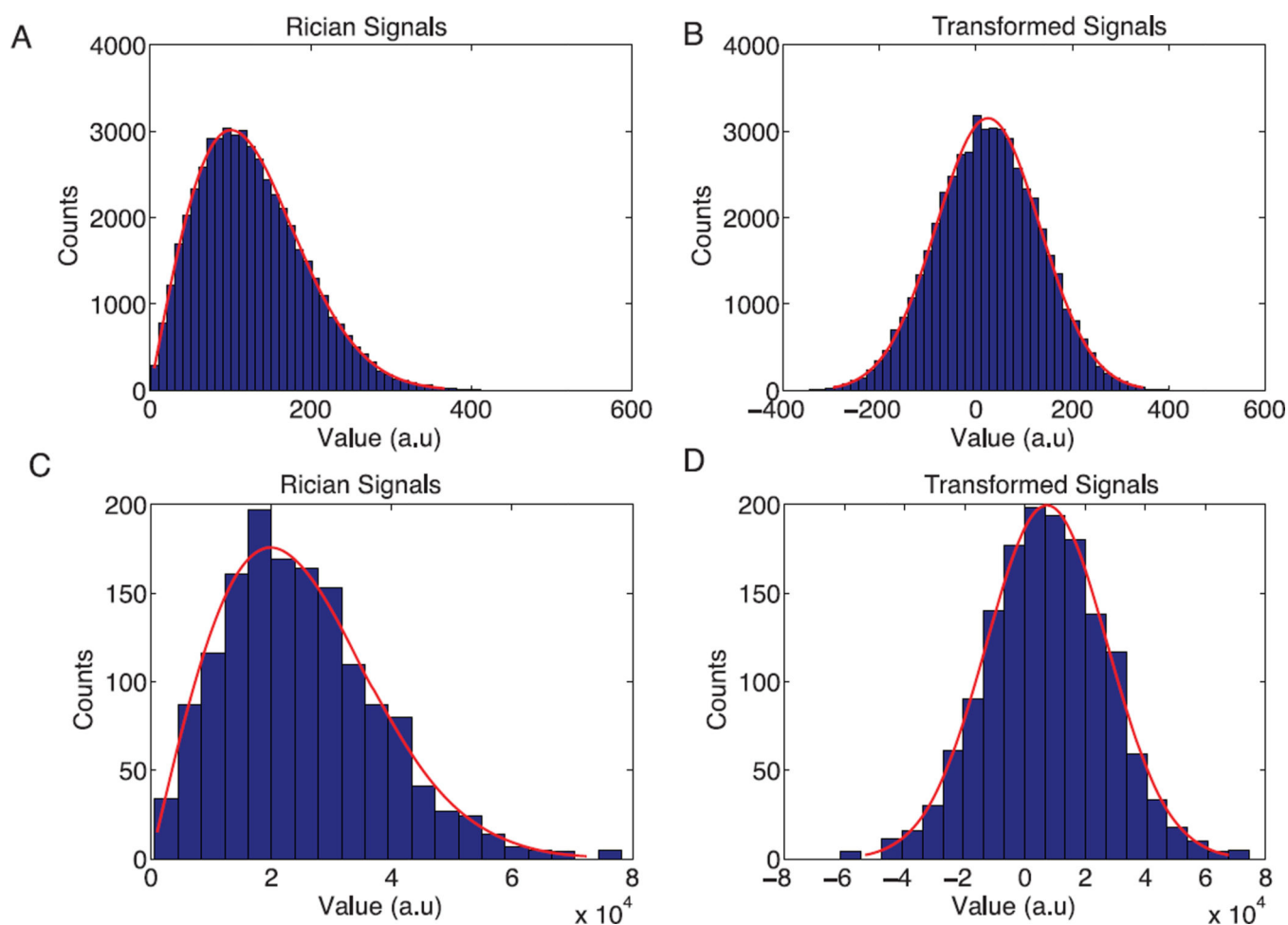


Fig. 4.

Histograms of the noisy magnitude signals (A, C) and their transformed values (B, D) of the simulation data at $TE = 200\text{ms}$ (A, B) and short- T_2 gel MRI data at $TE = 140\text{ms}$ (C, D). The red curves are the fittings to Rician distributions (A, C) and Gaussian distributions (B, D).

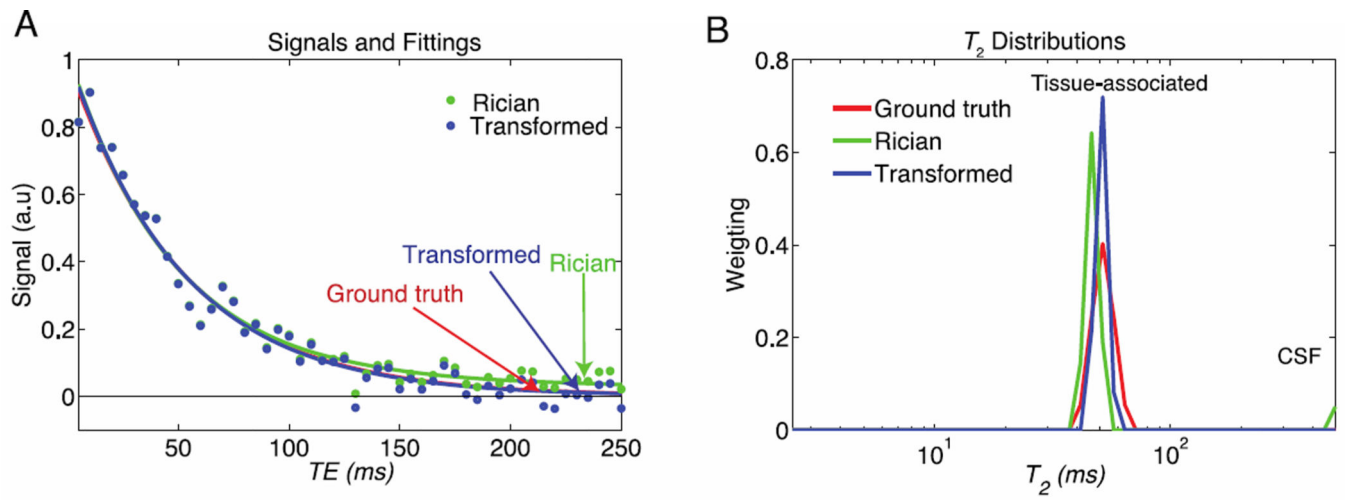


Fig. 5.

An example of the simulations with a single T_2 component at iSNR = 25. (A) The noisy magnitude signals (green dots) and the transformed signals (blue dots). The green and blue continuous curves are the fitting results obtained with the NNLS algorithm. (B) The T_2 distribution using the original Rician signals (green) and the transformed signals (blue). The continuous red curve in both (A) and (B) is the ground truth.

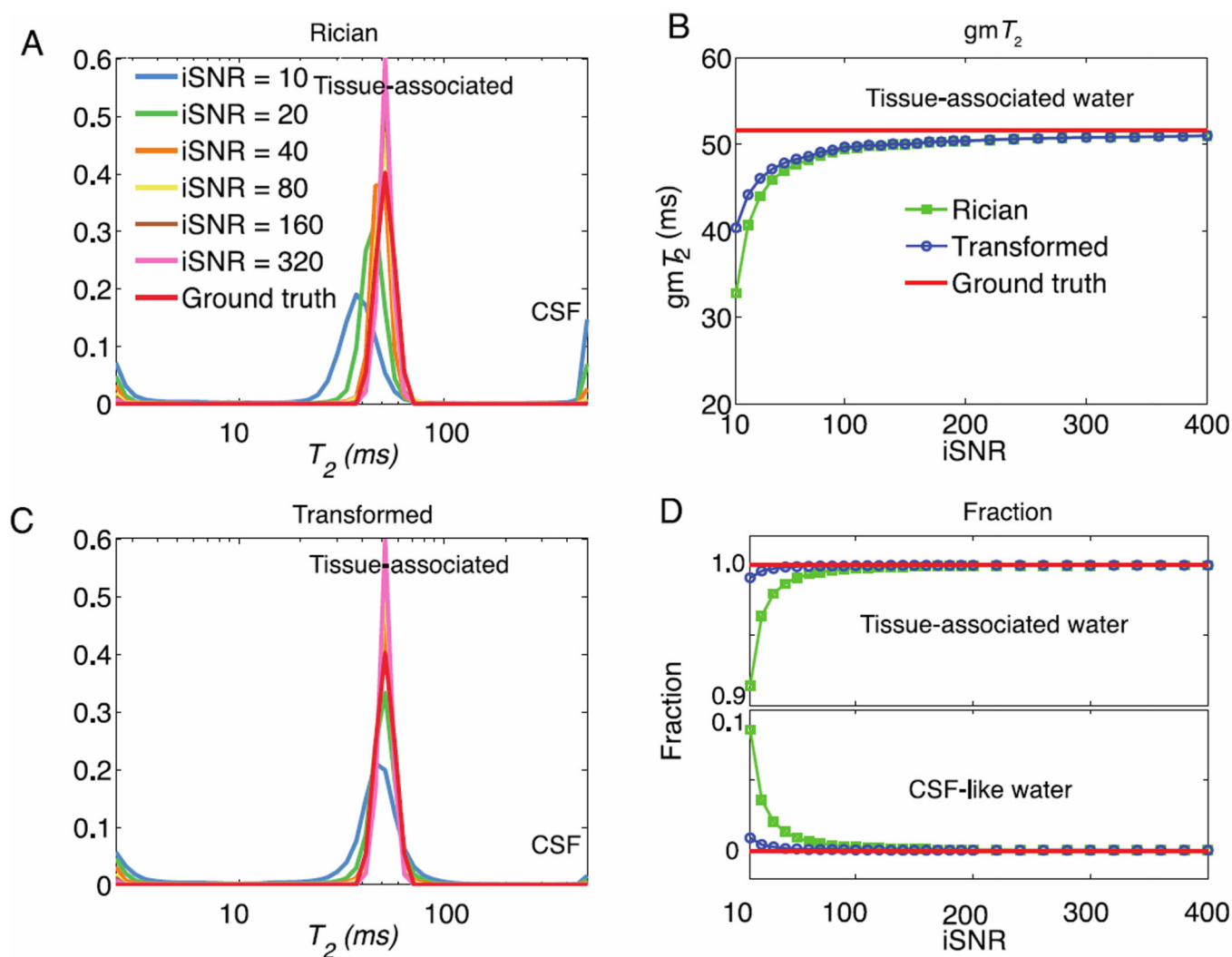


Fig. 6. T_2 distributions using the Rician signals (A) and the transformed signals (C) at various iSNR. The gmT_2 values of the tissue-associated water (B) and the relative fractions of both the tissue-associated water and the CSF-like water (D) were plotted as a function of iSNR.

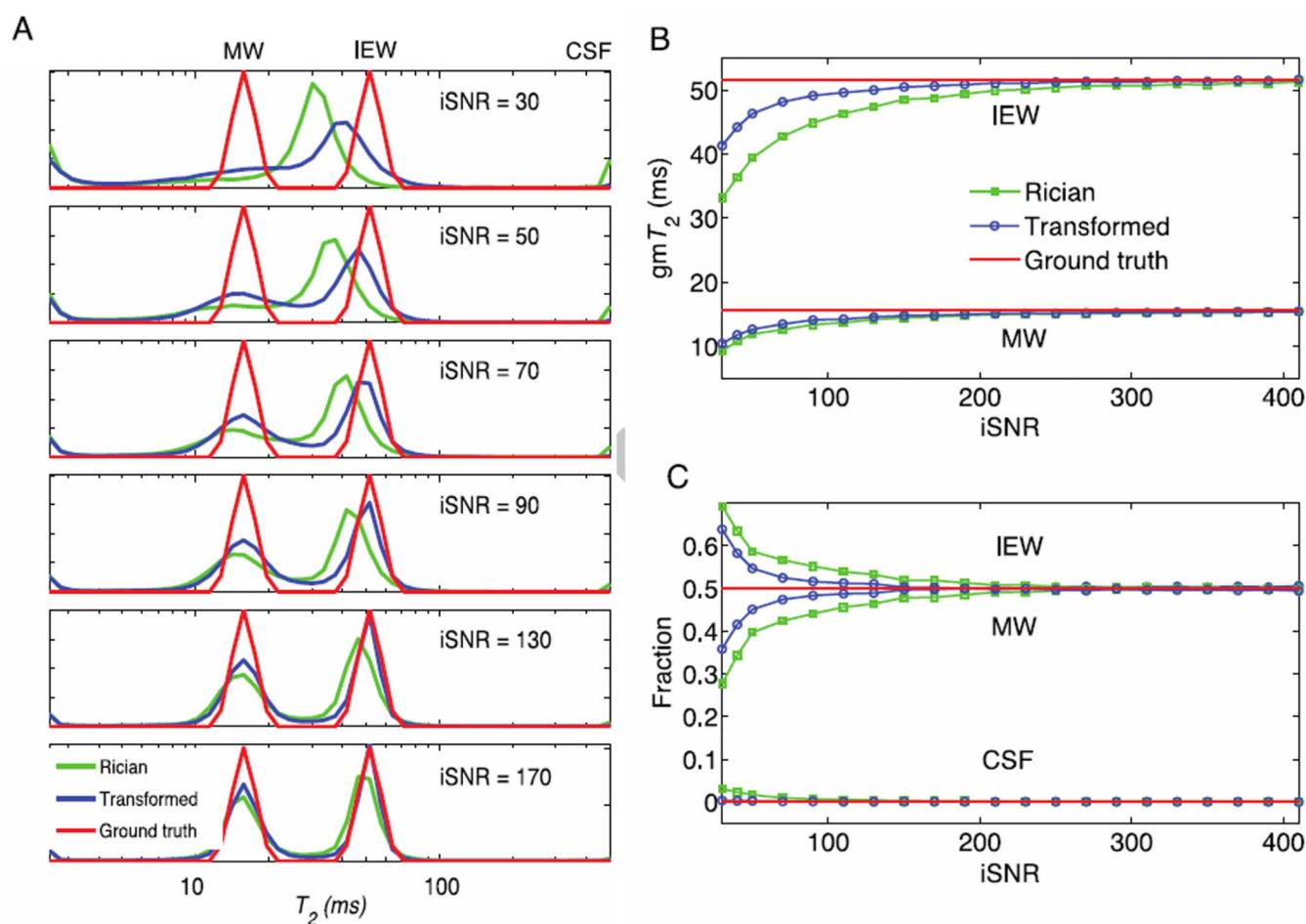


Fig. 7. (A) The T_2 distributions of the simulations of two T_2 components with various iSNR and their corresponding gmT_2 values (B) and relative fractions (C) of different regimes. The red curves in (A–C) are the underlying ground truth.

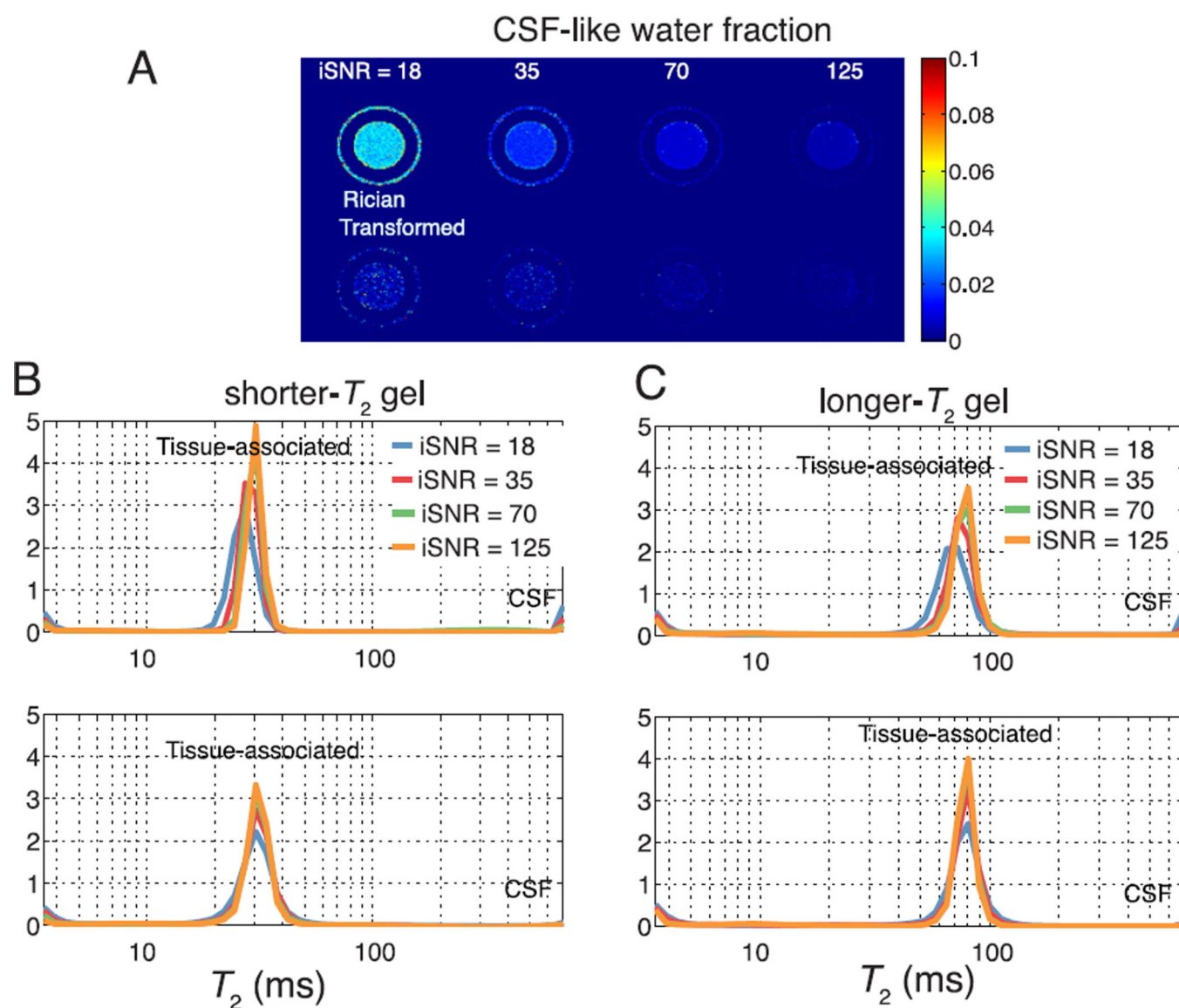


Fig. 8.

(A) Maps of the relative fractions of the CSF-like water with various iSNR. (B–C) T_2 distribution of the shorter- T_2 gel (B) and the longer- T_2 gel (C) with various iSNR.

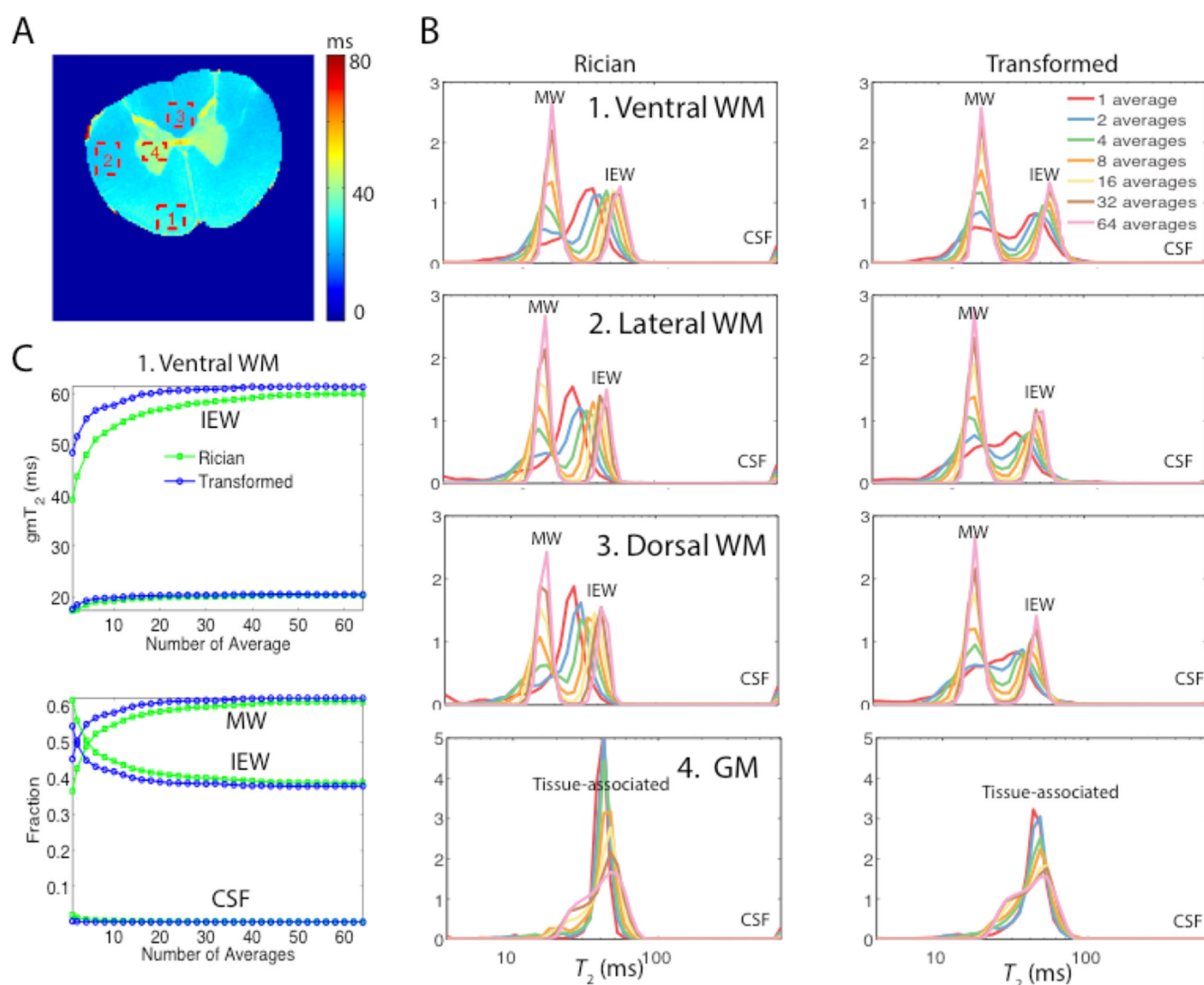
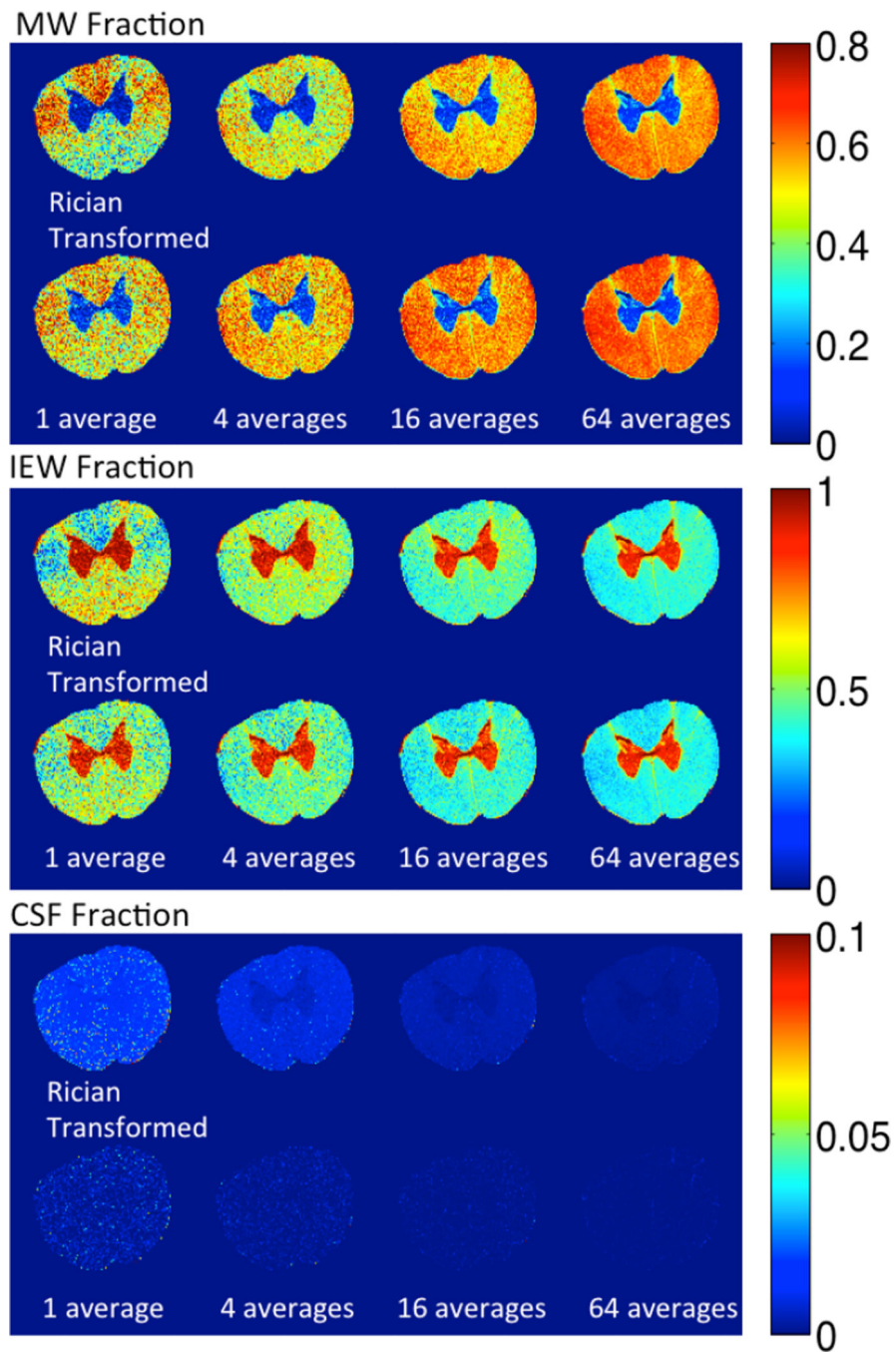


Fig. 9. (A) The map of the gmT₂ from 3.5ms–700ms of the spinal cord. (B) The T₂ distributions of the four ROIs (ventral WM, lateral WM, dorsal WM, and GM) with 1, 2, 4, 8, 16, 32 and 64 averages of the complex data using the original magnitude signals and the transformed signals. (C) The gmT₂ and relative water fractions of different water components in the ventral WM as a function of the number of averages.

**Fig. 10.**

The maps of the relative water fraction of MW (top), IEW (middle), and CSF (bottom) in the spinal cord with the number of averages of the complex data equal to 1, 4, 16 and 64.

Table 1

Statistic results of the gm T_2 values and relative fractions for the agar gel phantom

Number of Averages		1	4	16	50
<i>shorter-T_2 gel</i>					
Rician signals	Tissue-associated	24.8ms (96.5%)	27.1ms (98.2%)	28.2ms (99.1%)	28.5ms (99.5%)
	CSF-like	3.5%	1.8%	0.9%	0.5%
Transformed signals	Tissue-associated	27.5ms (99.4%)	28.2ms (99.7%)	28.5ms (99.8%)	28.7ms (99.9%)
	CSF-like	0.6%	0.3%	0.2%	0.1%
<i>longer-T_2 gel</i>					
Rician signals	Tissue-associated	57.5ms (95.6%)	61.5ms (98.5%)	63.3ms (99.6%)	63.8ms (99.8%)
	CSF-like	4.4%	1.5%	0.4%	0.2%
Transformed signals	Tissue-associated	63.1ms (99.4%)	63.3ms (99.8%)	63.7ms (99.9%)	63.9ms (99.9%)
	CSF-like	0.6%	0.2%	0.1%	0.1%